



# Role of in-situ electro-generated $\text{H}_2\text{O}_2$ bridge in tetracycline degradation governed by mechanochemical Si-O anchoring $\text{Cu}^{2+}$ as electron shuttle during E-peroxone process

Shangyi Li, Jun Huang<sup>\*</sup>, Yujue Wang, Gang Yu

State Key Joint Laboratory of Environment Simulation and Pollution Control (SKLESP), Beijing Key Laboratory for Emerging Organic Contaminants Control (BKLEOC), Beijing Laboratory for Environmental Frontier Technologies (BLEFT), School of Environment, Tsinghua University, Beijing 10084, China

## ARTICLE INFO

### Keywords:

Heterogeneous E-peroxone  
Anchored Cu  
Tetracycline  
Electron transfer  
Interface complex

## ABSTRACT

The efficient mineralization of tetracycline (TC) and reaction mechanism were investigated by designing heterogeneous  $\text{H}_2\text{O}_2$  bridge linked with active sites in higher valency species.  $\text{CuSi-BM}_{60}$  was synthesized by anchoring  $\text{Cu}^{2+}$  on Si-O functional groups of MCM-48 by mechanochemical technology to assist electro-peroxone treatment (E-peroxone). Results suggested that catalysts as electron shuttle enhanced electron transfer and reactive oxygen species (ROSs) generation, showing a complete tetracycline (TC) degradation and excellent mineralization (73.2%, 60 min). Cu sites significantly raised the interaction with in-situ electro-generated  $\text{H}_2\text{O}_2$ , generating uneven electron cloud distribution by Si-O...Cu...HO-OH<sup>\*</sup> bonding bridge, which enlarged H-O bonding length/angle near Cu and decreased orbital energy level gap. This work provided new insights into the complex of ball milling mediated  $\text{Cu}^{2+}$  with  $\text{H}_2\text{O}_2$  accompanied by the cycle of H-O bonding cleavage and regeneration for efficient ROSs production during E-peroxone.

## 1. Introduction

Pharmaceuticals and personal care products (PPCPs) were extensively used in treating human diseases and rearing livestock, and the majority of PPCPs was excreted into the environment via urine and feces [1]. Frequently, antibiotic residues were determined in the concentrations of ng/L to  $\mu\text{g/L}$  in the freshwater bodies [2]. Unfortunately, it was reported that higher concentrations of individual PPCPs in concentration from 40 to 50 mg/L were detected in the leachates of landfills in Oklahoma [3]. Furthermore, the concentrations of antibiotics (as high as  $\sim\text{mg/L}$ ) in pharmaceutical manufactories wastewaters were obviously higher than those of sewage or livestock effluents [4]. As one of the most common antibiotics, TC has been widely used in animal husbandry, agriculture and medicine, leading to long residual time in the environment and potential risk to human health [5]. Other researchers found that extremely high levels (844–1077 mg/L) could be detected in TC mother liquor, while that in wastewater treatment plants reached up to from several to dozens of mg/L even after dilution [6].

To minimize potential impacts of these substances to aquatic environment including pesticides and so on, effective treatment processes were urgently needed during water and wastewater treatment [7–10].

Ozonation could be used in combination with other advanced oxidation processes (AOPs) to enhance the degradation of refractory organic substances such as electrolysis, ultrasound, UV,  $\text{H}_2\text{O}_2$ , and persulfate [11–16]. In particular, an environmentally-friendly E-peroxone process has a synergetic effect on the ROSs generation due to the reaction between  $\text{O}_3$  and  $\text{H}_2\text{O}_2$  by coupling with in situ cathodic  $\text{H}_2\text{O}_2$  formation from oxygen ( $\text{O}_2$ ) reduction using carbon-based cathode via 2-electron pathway [17,18]. For one thing, E-peroxone could improve  $\text{O}_2$  utilization in the sparged gas mixture of  $\text{O}_3$  and  $\text{O}_2$ , which was the predominant gas (90–95% V/V) even if through the ozone generator; for another, in situ  $\text{H}_2\text{O}_2$  generation avoided the addition of external expensive chemical and safety accidents owing to the storage, transportation and handling of solutions compared with the conventional  $\text{O}_3/\text{H}_2\text{O}_2$  process [19]. Thus, E-peroxone process by installing electrodes in ozone reactors can be emerged as one promising AOP option for satisfyingly enhancing the emerging contaminants (EC) abatement in wastewater treatments. Meanwhile, the reaction mechanism of E-peroxone should be further investigated prior to its practical applications [20–22].

While the E-peroxone could improve EC elimination as compared to the individual process, a number of drawbacks were gradually revealed

<sup>\*</sup> Corresponding author.

E-mail address: [huangjun@mail.tsinghua.edu.cn](mailto:huangjun@mail.tsinghua.edu.cn) (J. Huang).

<https://doi.org/10.1016/j.apcatb.2021.120930>

Received 23 August 2021; Received in revised form 9 November 2021; Accepted 12 November 2021

Available online 19 November 2021

0926-3373/© 2021 Elsevier B.V. All rights reserved.

in term of the peroxone based degradation experiments due to  $\text{HO}_5^-$  adduct formation between the reaction of  $\text{O}_3$  with  $\text{HO}_2^-$ , which resulted in that the  $\bullet\text{OH}$  generation efficiency was only fifty percent of that proposed by the stoichiometry [23]. Furthermore, most of reported E-peroxone processes were performed in the homogeneous system except inserting the dual electrodes, and although the synergistic effect of electrolysis and ozonation treatment has been demonstrated, it still has the defect of low electron transfer and mass conductivity rate. To achieve “Kill two birds with one stone” strategy in E-peroxone, could the specialty designed catalysts help to overcome such a drawback of the limited mass transfer and enhance ROSs generation on the interface of solid-gas-liquid three phase in the meantime? Adsorption coupling with E-peroxone may be a promising candidate for solving this problem. Based on this, spinel ferrites modified carbon nanotubes ( $\text{CuFe}_2\text{O}_4/\text{CNTs}$ ) were fabricated and evaluated for fluconazole degradation during catalytic E-peroxone oxidation because of their stable crystalline structure, high magnetic response capability and catalytic activity [24]. The effects of operational and water quality parameters were investigated and found that approximately 89% fluconazole was transformed in the  $\text{CuFe}_2\text{O}_4/\text{CNTs}$  catalytic E-peroxone process. Most studies have focused on the target contaminant degradation and high mineralization was difficult to come it true or be ignored. Unfortunately, generated intermediate products could show the high environmental health risks during reaction. Moreover, the reaction mechanism and relationship between interface electron transfer and ROSs along with in-situ electro-generated  $\text{H}_2\text{O}_2$  in the heterogeneous catalytic E-peroxone should be deeply investigated.

Rich Si-O-Si and Si-OH functional groups in the framework of silica based mesoporous molecular sieves could be the anchoring site for transition-metal oxides including MCM-41 with two-dimensional pore or MCM-48 with three-dimensional pore channels and so on, which were the promising E-peroxone catalysts in this heterogeneous catalytic system [25–28]. The effective interface boosting electron transfer by electron shuttle based on chemical bonding was the key to enhance  $\text{O}_3$  chain reaction. Previous study has demonstrated that low valency of metal species formed by introducing additional elements as composites on the carriers was prone to create synergistic effect to lead to more ROSs generation [29,30]. It has been noted that binary metals oxidation cycling through a  $\text{Me}_1^{n+}/\text{Me}_1^{n+1}$  coupling with  $\text{Me}_2^{n+}/\text{Me}_2^{n+1}$  exhibited very large contributor to AOPs for EC degradation [31–34]. However, the related report about the role of high-valence active sites as bonding bridge on the interface electron transfer are very few, especially in the complex ozonation process. Therefore, we posit another strategy: was it available to design Si-O anchoring metal oxides with high-valence charges as electron shuttle to achieve better catalytic oxidation performance?

Theoretically, ball milling process due to ball-to-powder collisions could lead to super high temperature ( $>1000^\circ\text{C}$ ) at some local area (ca.  $1\ \mu\text{m}^2$ ) in very short time ( $10^{-3}$ – $10^{-4}$  s) when synthesizing materials [35]. Such high energy input was sufficient to stimulate chemical reaction at the solid-solid interface and thus reactions from mechanochemical mixing may have novel characteristics. Metal oxides with abundant oxygen vacancies could be rapidly increased via the dislodging of surface  $\text{O}_{\text{lattice}}$  after ball milling treatment, which could outperform their counterparts synthesized by conventional solvent-based routes [36]. In this technique, repeated collision and friction of ball also caused mechanical deformations and introduced other high-density surface defects on metals. Hence, the crystallites fracture of metal oxides into smaller pieces could be down to the nanometer range. In addition, incorporation of oxygen into the bulk of the sample upon milling could occur especially in the atmosphere of air. Previous study showed that the clean Cu surfaces created by the powder fracturing process might react with oxygen [37]. The input of energy can promote the reaction among different reagents and an excess amount of energy would lead to over-oxidation and this unique phenomenon would change the valency of metal sites [38,39]. Furthermore, ball milling was

a green method to develop efficient and low-cost catalysts under the solvent-free system, avoiding the highly specialized and expensive equipment manufacture for preparing.

Therefore, we devised the Cu species with high valence states anchoring on the Si-O of MCM-48 by using green ball milling method in air environment. Meanwhile, in situ electrochemical characterization, X-ray absorption spectroscopy (XAS) and density functional theory (DFT) calculation were employed to investigate the reaction mechanism of interface complex with  $\text{H}_2\text{O}_2$  from E-peroxone and high-valence initiated electron transfer.

## 2. Experimental section

### 2.1. Chemical reagents

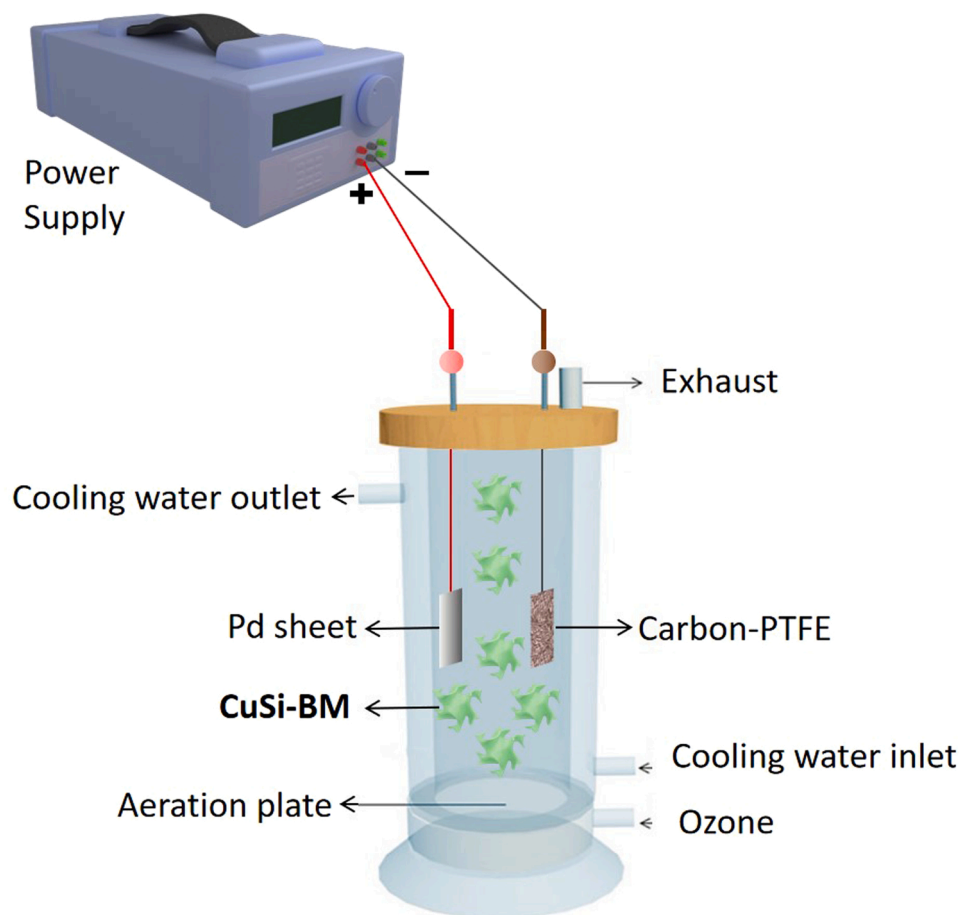
The chemical reagents were shown in [Supplementary Material S1](#) in the [Supplementary Information](#).

### 2.2. Catalysts preparation and characterization

MCM-48 sphere inserted by Cu nanorods was prepared by one-pot hydrothermal method. Briefly, 6.1 g CTAB@MCM-48 was synthesized by adding CTAB and 15 mL TEOS in NaOH solution (0.75 M, 70 mL) at room temperature. Then 0.187 g cooper nitrate trihydrate was mixed with above CTAB@MCM-48 gel in at room temperature and it was poured into 200 mL autoclave after 4 h reaction, followed by at 3 days for crystallization in  $100^\circ\text{C}$  oven. The heated autoclave was cooled down to room temperature about 6 h and the layered gel was filtrated and washed by 1500 mL ultrapure water and 100 mL ethanol. Then, the mixture was dried in  $100^\circ\text{C}$  oven. Finally, the light blue powder was transferred to a Muffle furnace for calcination at  $500^\circ\text{C}$  for 5 h in an air flow with a heating rate of  $1^\circ\text{C}\ \text{min}^{-1}$ . The ball milling for the active nanoparticles grown along with the bonding bridge of Si-O was carried out in a Pulverisette-7 planetary ball mill (Fritsch, Germany) with a stainless-steel pot (80 mL) with 25 stainless steel balls (10 mm in diameter) at different rotational speed and time before calcination. The schematic diagram of sample synthesis was exhibited in [Fig. S1](#). The process of carbon-polytetrafluoroethylene cathode (carbon-PTFE) electrode synthesis was described in [Supplementary Material S2](#). The characterization of catalysts and DFT calculation method were respectively shown in [Supplementary Material S3](#) and [S4](#) in the [Supplementary Information](#).

### 2.3. Catalytic E-peroxone procedure

Ozonation, E-peroxone, heterogeneous catalytic ozonation,  $\text{O}_3$ -electrolysis, and heterogeneous E-peroxone treatment of 500 mL TC solution were conducted in a cylindrical reactor at room temperature, as depicted in [Scheme 1](#). Before experiments, 10 mg/L of TC wastewater was prepared to simulate the actual TC concentration in swine and pharmaceutical wastewater according to previous study [6,40,41]. The standard laboratory ozone generator at 100 mg/h was used to produce  $\text{O}_3$  from high-purity  $\text{O}_2$  gas (OzoneLab™ OL80 (90° panel series), made in Canada). The distance between the anode and cathode was 2 cm with an exposed area of  $10\ \text{cm}^2$ . The supporting electrolyte was a 0.05 M  $\text{Na}_2\text{SO}_4$  solution under galvanostatic conditions using a DC power supply. For  $\text{O}_3$ -electrolysis, the treatment was like E-peroxone process except that the carbon-PTFE electrode was replaced with a stainless steel (SS) plate. 100 mg of catalysts were added in the above solution to trigger the heterogeneous E-peroxone reactions. 25 mL of liquid samples were drawn by a single-use sterile syringes and filtered through  $0.45\ \mu\text{m}$  membrane. TC concentration was quantified by a UV-Visible Spectrophotometer at  $\lambda = 360\ \text{nm}$ . TOC was measured using a TOC-VCPH analyzer (Shimadzu Co. Japan). The concentration of  $\text{H}_2\text{O}_2$  was determined by using potassium titanium (IV) oxalate method [42].  $\text{H}_2\text{SO}_4$  solution (3 M) was used to adjust the sample pH to prevent the



**Scheme 1.** Illustration of the heterogeneous E-peroxone process.

interference of  $O_3$  with  $H_2O_2$  measurement [43]. And it could be detected at  $\lambda = 402$  nm after 5 min completed reaction. Ultra-Performance Liquid Chromatography Tandem Mass Spectrometry (UPLC/MS/MS) analysis was performed to detect the intermediate products during reaction in [Supplementary Material S5](#).

### 3. Results and discussion

#### 3.1. Physicochemical properties of the catalysts

X-ray diffraction (XRD) was displayed to characterize the compositions and phase of Cu modified catalysts as different ball milling time in [Fig. 1\(a\)](#). The CuO noticeable signals positioned at  $35.5^\circ$ ,  $38.7^\circ$ ,  $48.6^\circ$  and  $66.1^\circ$ , which were separately assigned to the  $(-111)$ ,  $(111)$ ,  $(-202)$  and  $(-311)$  plane (JCPDS46-1548). In addition, the weak peaks located at  $61.5^\circ$ ,  $73.5^\circ$  and  $77.3^\circ$  indexed to diffraction of the different planes of low state of Cu oxides species [44]. The crystalline structure of  $Cu_2O$  and CuO was shown in [Fig. 1\(b\)](#). Meanwhile, in contrast with CuSi-BM<sub>0</sub>, the mechanically milled as-prepared MCM-48 anchoring CuO broke slightly the order degree of the 3D pore structure in the CuSi-BM<sub>60</sub> samples, as confirmed by the decreased peak intensity of  $2\theta = 3.02$  in low-angle XRD patterns presented in [Fig. S2](#). [Fig. 1\(c1\)](#) displayed the nitrogen adsorption isotherms to study the variation of structural properties of the CuSi-BM<sub>0</sub> and CuSi-BM<sub>60</sub>. According to [Fig. 1\(c2\)](#), (c3) and (c4), the BET surface area and pore volume were enhanced from 1005.43 to 1062.03  $m^2/g$  and from 0.72 to 0.78  $cm^3/g$  after 1 h of milling process, respectively. The reason may be that the high collisions between balls and martite particles in the planetary ball milling led to the reduction and transformation of a part of micron scale particles of copper sites to nano scale and consequently a slightly increase in BET surface area and

pore volume could be observed. Furthermore, greater surface area could be attributed to the decreased average pore size of CTAB@Cu-MCM-48, which may result in the enhanced reactivity of CuSi-BM<sub>60</sub>. The SEM, TEM images and EDS analysis showed a large amount of CuOx nanorods grown on the MCM-48 silica sphere, which were exhibited in [Fig. 1\(d-f\)](#). It could be observed in the microscopic morphology of CuSi-BM<sub>60</sub> that the Si sphere was slightly damaged during ball milling, which agreed with the results of XRD. Taken from the single nanorod in the results of HRTEM showed that the Cu decorated mesoporous composites had some well resolved lattice fringes distances which were measured to be 0.235 nm, corresponding to the high exposure of CuO (111) crystal planes ([Fig. 1\(g\)](#)).

Py-IR measurements results showed that catalysts all emerged three distinct peaks at 1443, 1572, and 1608  $cm^{-1}$  represented Lewis acidic sites, while the peak at 1490  $cm^{-1}$  could be ascribed to coexistence of Lewis and Brønsted acid sites in [Fig. S3\(a\) and \(b\)](#) [45]. The surface Lewis acid sites were improved in CuSi-BM<sub>0</sub> in contrast with CuSi-BM<sub>60</sub> due to the role of  $Cu_2O$  in the low valency state of catalysts [46]. Furthermore, the  $H_2$ -TPR of samples implied that CuSi-BM<sub>60</sub> with the first step where  $[Cu^{2+}]$  was reduced to  $[Cu^+]$  species showed a stronger intensity of peak than CuSi-BM<sub>0</sub> in the temperature range 150–350  $^\circ C$ , attributing to higher CuO contents production in [Fig. S4](#) [47,48]. X-ray photoelectron spectroscopy (XPS) analysis was performed to confirm surface chemical property of active sites, which was shown in [Fig. S5\(a\) and \(b\)](#). The binding energy peaks centered at 932.9 eV (Cu 2p<sub>3/2</sub>) together with 952.6 eV (Cu 2p<sub>1/2</sub>) were respectively corresponded to low state of copper  $[Cu^+]$  or  $[Cu^0]$  [49]. Peaks centered at 934.9 eV (Cu 2p<sub>3/2</sub>) and 954.9 eV (Cu 2p<sub>1/2</sub>) along with the satellite peaks at 942.9 eV and 962.8 eV belong to the  $d^9$  electron configuration of high state of Cu are ascribed to  $[Cu^{2+}]$  [50]. It was worthwhile noting that the



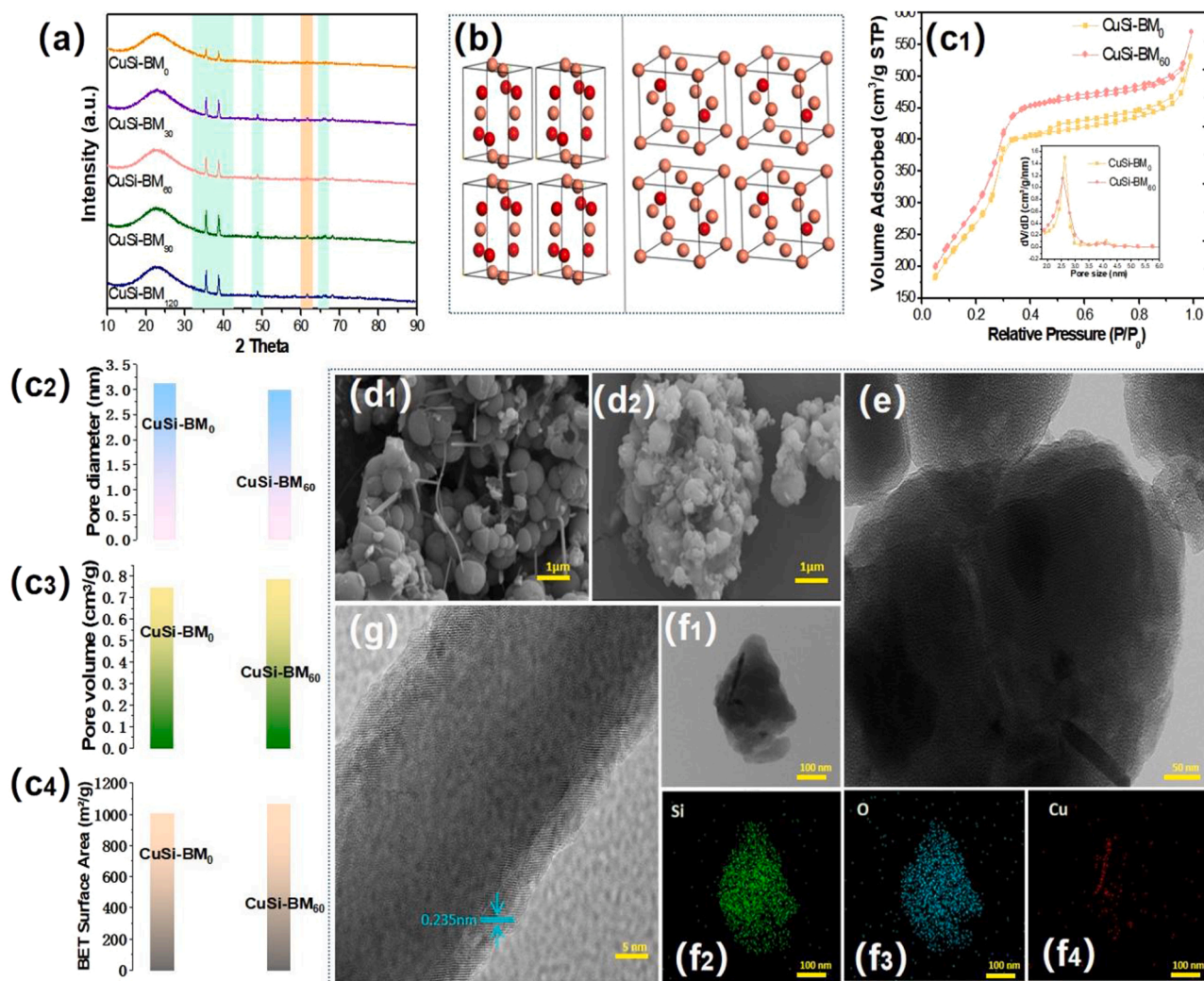


**Fig. 1.** (a) XRD patterns of catalysts during different ball milling time. (b) Crystalline structure of Cu<sub>2</sub>O (left) and CuO (right). (c1) N<sub>2</sub> adsorption-desorption isotherms and pore size distribution (inserted), (c2) pore diameter, (c3) pore volume, (c4) BET surface area measurements of CuSi-BM<sub>0</sub> and CuSi-BM<sub>60</sub>. The red and salmon pink spheres are O, Cu atoms, respectively. SEM images of (d1) CuSi-BM<sub>0</sub> and (d2) CuSi-BM<sub>60</sub>. (e) TEM images of CuSi-BM<sub>60</sub>. (f1)-(f4) EDS mapping images of CuSi-BM<sub>60</sub>. (g) HR-TEM images of CuSi-BM<sub>60</sub>. (For interpretation of the references to color in this figure legend, the reader is referred to the web version of this article.)

ratios of [Cu<sup>+</sup>] or [Cu<sup>0</sup>] to [Cu<sup>2+</sup>] on CuSi-BM<sub>0</sub> were obviously higher than CuSi-BM<sub>60</sub>. And it indicated that CuSi-BM<sub>60</sub> possessed the higher [Cu<sup>2+</sup>] ratio due to the mechanochemistry effect, which was consistent with the results of H<sub>2</sub>-TPR. Meanwhile, EPR technique was undertaken to explore the electronic paramagnetic signal of the Cu modified silica based mesoporous molecular sieves before and after ball milling. A weak signal could be observed from Fig. S6 on the EPR spectra of the CuSi-BM<sub>0</sub> at the magnetic field value (G) = 3160, indicating that only small number of unpaired electrons existed on the modified catalysts without mechanical force. However, upon the introduction of ball milling, Cu modified Si-O catalysts exhibited a stronger EPR signals, clearly confirming that rich unpaired electrons with characteristic [Cu<sup>2+</sup>] existed around the introduced metal species. Apparently, the appearance of the strong EPR signal can be in close connection with the enhanced unpaired electrons around the incorporated Cu after ball milling, which was a result of the enhanced [Cu<sup>2+</sup>] and coordinative Si-O bridge interactions, and thus an improved E-peroxone based heterogeneous interface could be observed.

Normalized X-ray absorption near edge structure (XANES) spectra of different samples at the Cu K-edge of was shown in Figs. 2(a) and S7(a), along with those of standard samples including Cu foil, CuO<sub>2</sub> and Cu<sub>2</sub>O, indicating that the Cu atoms in CuSi-BM<sub>0</sub> and CuSi-BM<sub>60</sub> existed as a

partially positively charged mixture (Cu<sup>δ+</sup>, 0 < δ < 2). The position of white line for catalysts was located between Cu foil and CuO, demonstrating that the valence state of Cu in the two samples was situated between [Cu<sup>0</sup>] and [Cu<sup>2+</sup>] species. It could be found that the white-line intensity of CuSi-BM<sub>60</sub> was much higher than that of CuSi-BM<sub>0</sub>, indicating that Cu species was in the higher average valence state of oxidized forms in CuSi-BM<sub>60</sub>, which was corresponded to the fitting results of XPS. According to the EXAFS results through a Fourier transformation, the Cu–O (1.4–1.5 Å) and Cu–Cu (2.4–2.8 Å) coordination peaks were separately assigned to the first and second shell of samples in Figs. 2(b), (c), (d), S7(b), (c), S8 and Table S1. For CuSi-BM<sub>0</sub> and CuSi-BM<sub>60</sub>, three scattering paths were used to fit the data including a short Cu–O path (Cu–O<sub>1</sub>), a long Cu–O path like that of the second neighbor Cu–O path in CuO with different distances and the Cu–Cu path from metallic Cu. The similar prominent peak with standard samples were corresponding to the Cu–O and Cu–Cu coordination. And the first Cu–O<sub>1</sub> shell derived from the Cu–O bonds with a coordination number (CN) of 2.8 and 3.2, respectively, along with an average bond distance (R) of 1.95 Å, implying that loss of Cu–O coordination was attributed to Si–O anchoring in the complex clusters in contrast with standard CuO (4). In contrast to CuSi-BM<sub>0</sub>, the increased CN of Cu–O<sub>1</sub> in CuSi-BM<sub>60</sub> by ball milling was closer to the high valency of Cu, which was probably the essence of



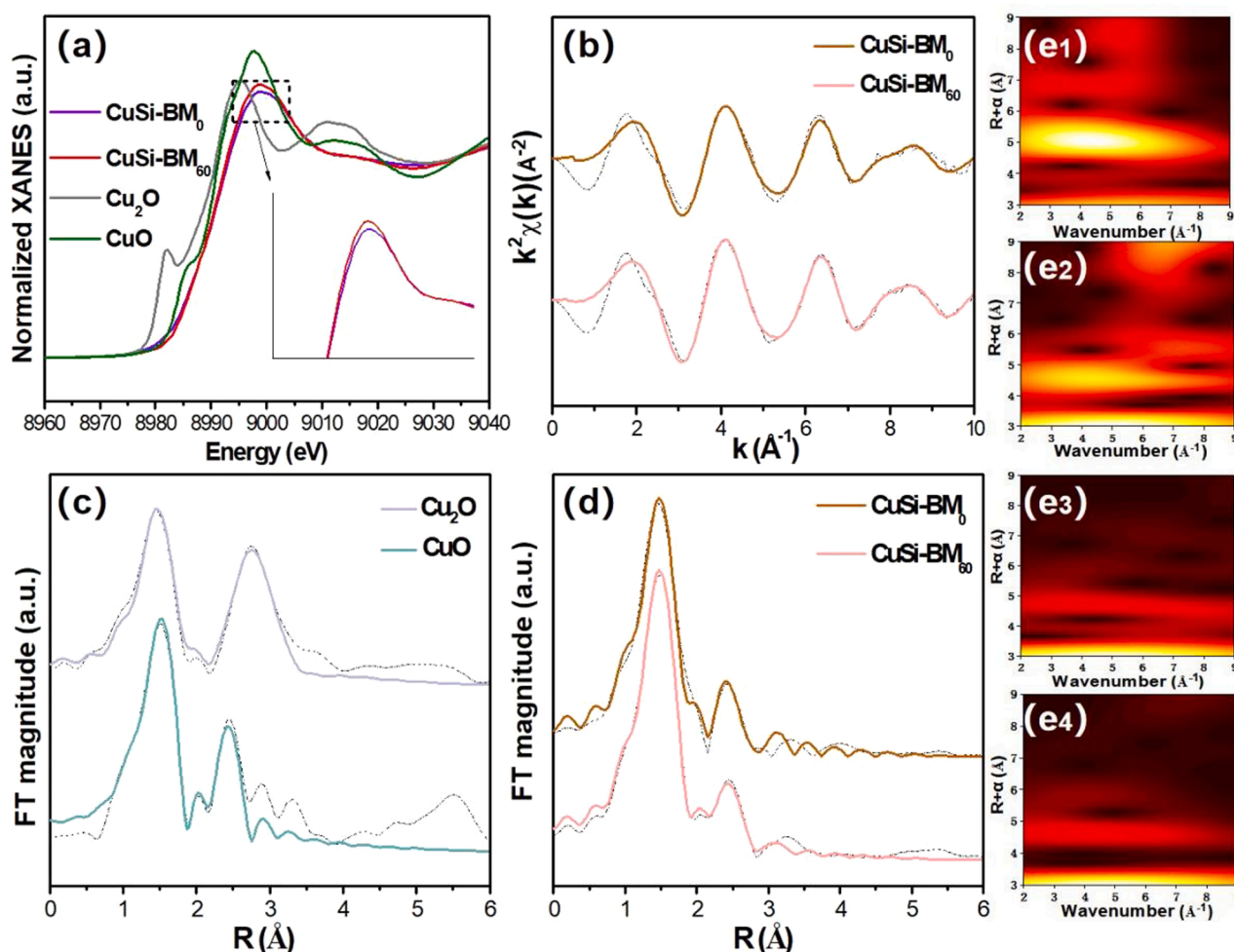


Fig. 2. (a) The Cu K-edge XANES spectra of the samples. (b) The curve fitting in K-space from the Cu K-edge EXAFS spectra of CuSi-BM<sub>0</sub> and CuSi-BM<sub>60</sub>. (c) The curve fitting in R-space from the Cu K-edge EXAFS spectra of standard Cu<sub>2</sub>O and CuO. (d) The curve fitting in R-space from the Cu K-edge EXAFS spectra of CuSi-BM<sub>0</sub> and CuSi-BM<sub>60</sub>. Wavelet transform 3D image of (e1) standard Cu<sub>2</sub>O, (e2) standard CuO, (e3) CuSi-BM<sub>0</sub> and (e4) CuSi-BM<sub>60</sub>.

improved catalytic efficiency and it echoed with the above results of characterization. Furthermore, we also found the decrease and increase in the Cu-Cu and Cu-O coordination under the mechanochemical effect, indicating that CuSi-BM<sub>60</sub> enhanced the interaction between Cu and O along with diminishment of Cu interatom forces in Cu clusters, respectively. The bond distances and coordination atoms of CuSi-BM<sub>0</sub> and CuSi-BM<sub>60</sub> were also investigated by wavelet transform 3D images in Figs. 2(e) and S9. It could be observed that rather than Cu foil, standard CuO or Cu<sub>2</sub>O showed similar distribution profiles with the catalysts. Meanwhile, the pattern of CuSi-BM<sub>60</sub> was much closer to CuO than CuSi-BM<sub>0</sub> owing to higher concentration of high valence state of Cu. The distribution profile of Cu-Cu and Cu-O was weakened at a longer distance owing to effective exposure of metal atoms in the Si-O sketch.

### 3.2. Enhanced E-peroxone process

Fig. 3(a) showed that TOC removal was rapidly enhanced from 64.2% to 73.2% after 60 min of catalytic E-peroxone when the initial current increased from 10 to 30 mA. In this case, more H<sub>2</sub>O<sub>2</sub> was generated and reacted with O<sub>3</sub> to produce ROSs due to enhanced the anodic oxidation and cathodic reduction. Furthermore, O<sub>3</sub> could be electro-reduced on electrode in the applied current range and turned into •OH, which was beneficial to TC mineralization. However, further increasing the current to 70 mA did not improve TOC elimination yet further. TOC conversion rate of TC gradually decreased from 67.9% to

52.2% with increasing cathodic current density from 50 mA up to 70 mA at 60 min treatment. This was attributed to that aqueous O<sub>3</sub> was insufficient to react with electro-generated H<sub>2</sub>O<sub>2</sub> in the higher current E-peroxone process and the residual H<sub>2</sub>O<sub>2</sub> would undergo the reaction that captured excessive •OH in bulk solution and thus decreased the catalytic efficiency [21,51]. Moreover, the associated increase on in-situ electro-generation of H<sub>2</sub> and O<sub>2</sub> at electrodes via water electrolysis could block the Cu active sites on CuSi-BM<sub>60</sub> and reduce the effective interface reaction region available. The contact angle tests were carried out to evaluate the hydrophobicity of carbon-PTFE electrode after 30 mA or 70 mA reaction in the CuSi-BM<sub>60</sub>/E-peroxone process in Fig. S10. The decreased water contact angle (102°) by the 70 mA treatment could signify that higher initial current might suppress the hydrophobicity of carbon-PTFE, which would inhibit gas affinity and oxygen microbubbles transfer on the electrode surface. The result was agreement with the declined TOC removal when the initial current further increased during electrochemical H<sub>2</sub>O<sub>2</sub> production with oxygen sparging.

TOC elimination from TC solutions by ozonation alone, E-peroxone, CuSi-BM<sub>0</sub>/E-peroxone, CuSi-BM<sub>60</sub>/O<sub>3</sub>-electrolysis and CuSi-BM<sub>60</sub>/E-peroxone process were compared in Fig. 3(b). The abatement of TOC was significantly accelerated after the change of conventional ozonation (15.5%) to the E-peroxone (44.8%) at 60 min reaction time, which could be attributed mainly to the enhanced O<sub>3</sub> transformation to •OH during the ROSs chain reaction in the presence of electro-generated H<sub>2</sub>O<sub>2</sub>. Notably, TOC removal was significantly improved when CuSi-BM<sub>0</sub> and

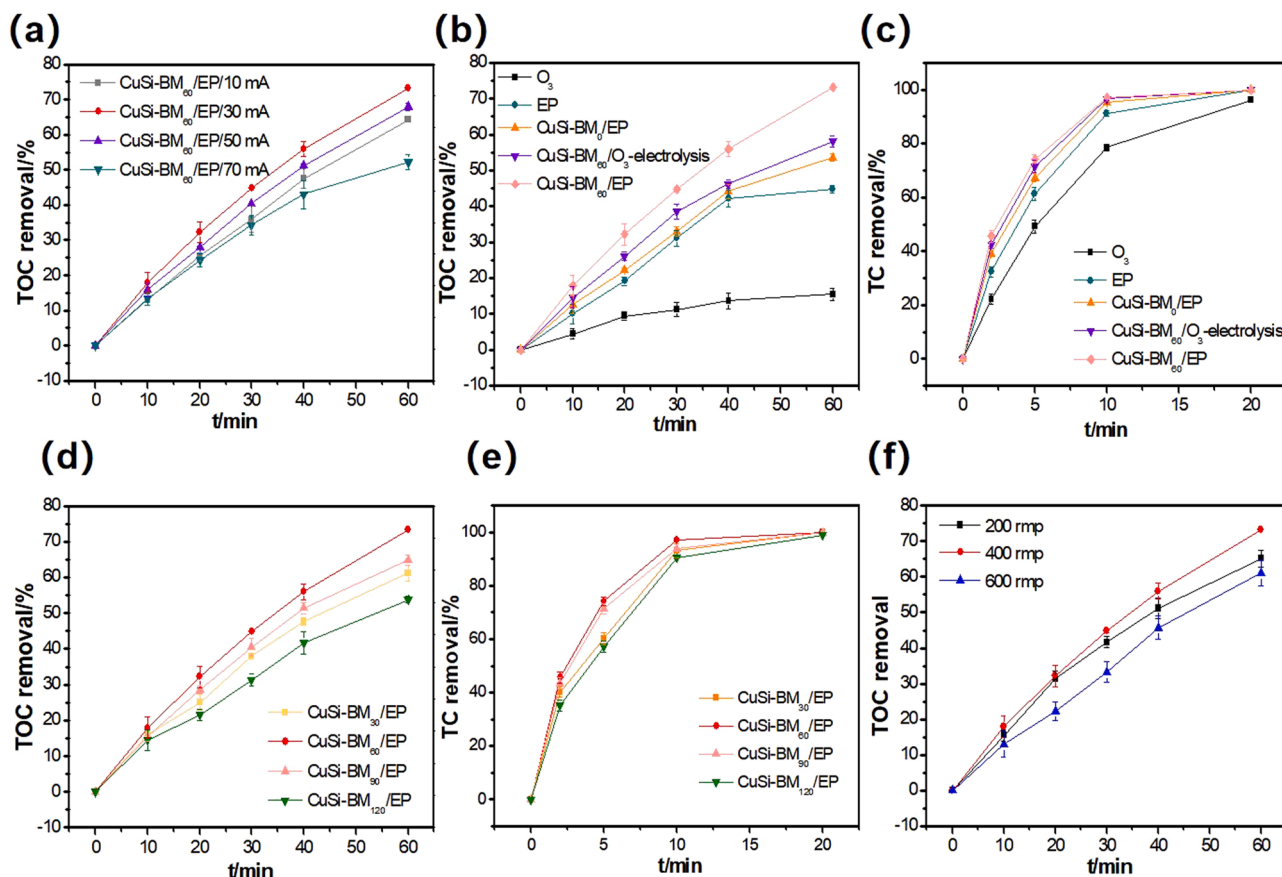


**Fig. 3.** (a) TC mineralization by heterogeneous E-peroxone in different applied current. (b) TC mineralization and (c) degradation in different reaction systems. (d) TC mineralization and (e) degradation by heterogeneous E-peroxone in different ball milling. Reaction conditions: [initial TC] = 10 mg L<sup>-1</sup>; volume = 500 mL; [catalysts] = 0.2 g L<sup>-1</sup> (if used), [inlet gas phase O<sub>3</sub>] = 7.5 mg/L (if used); sparging gas flow rate = 0.25 L/min; applied current = 30 mA, average cell voltage = 2.3 V; initial pH = 5.1.

E-peroxone were combined. For the heterogeneous E-peroxone process that used the CuSi-BM<sub>60</sub>, TOC removal reached 53.6% at 1 h. The introduction of the prepared catalysts into the ozonation system clearly enhanced TC mineralization. Furthermore, the ball milling process improved the catalytic performance of the Cu modified Si-O sketch in mesoporous molecular sieves. It was reasonable to infer that interface reaction played an important role in enhancing the E-peroxone. Meanwhile, carbon-PTFE cathode was replaced with a stainless-steel cathode (10 cm<sup>2</sup>) to evaluate the CuSi-BM<sub>60</sub>/electrolysis-O<sub>3</sub> process for TC degradation, and the results showed the heterogeneous electrolysis-O<sub>3</sub> process also considerably improved TOC elimination (58%) as compared to individual ozonation and E-peroxone processes at 60 min, which was attributed to the high concentration of •OH generation from O<sub>3</sub> decomposition and electro-reduction near the stainless-steel cathode. However, the improvement in target contaminant degradation achieved in the electrolysis-O<sub>3</sub> process was still lower than that obtained in the E-peroxone process. Therefore, electro-generated H<sub>2</sub>O<sub>2</sub> contributed more to the ROSs formation reaction than improved O<sub>3</sub> self-decomposition. The abatement of TC also showed similar trend with TOC removal and the results were exhibited in Fig. 3(c).

Fig. 3(d) showed the influence of different ball milling time on TC mineralization at the same constant rotation frequencies (400 rpm). It could be observed that the conversion rate of TOC gradually increased with increasing ball milling time, approximate 61.3% and 73.2% mineralization were observed at 60 min treatment for CuSi-BM<sub>30</sub> and CuSi-BM<sub>60</sub> catalysts. However, the further increase of the ball milling time to 90 and 120 min decreased the TC mineralization efficiency slightly. This result was in line with previous study that ball-milling of MWCNT (even for only 5 min) enhanced the catalyst performance for

oxalic acid ozonation and increased with the milling time up to 240 min, and then a slightly decrease could be observed [52]. Thus, the powder milled in 60 min was the best catalyst among these different ball milling treated samples, which may be explained by small particle sizes of the agglomerates and ordered mesoporous structure, where electro-generated H<sub>2</sub>O<sub>2</sub>, O<sub>3</sub> and TC could be adsorbed for the interface reaction. The decay in the efficiency of the catalyst milled during 90 and 120 min would be justified by the decrease in the order degree of mesoporous molecular sieves owing to the crooking, breaking and curving of some pore channels, which may lead to partially obstruct the access of TC, O<sub>3</sub> and H<sub>2</sub>O<sub>2</sub> to the three-dimensional pore, then decreased mass transfer performance. Similar trend could be observed during TC concentration removal in Fig. 3(e). Meanwhile, the effect of ball milling vibration frequency (200 rpm, 400 rpm and 600 rpm) was evaluated for the ball milling time of 60 min in Fig. 3(f). It was observed that the increase in the frequency slightly improved catalytic efficiency at 400 rpm (for values higher than 200 rpm) and significantly decreased TOC removal owing to the destroyed order degree of catalysts when it reached up to 600 rpm. Therefore, it seemed that the milling rotation frequency had a similar effect on the textural properties change of CuSi-BM<sub>60</sub> than the ball milling time.

Fig. 4(a) displayed that adsorption and adsorption-electrolysis of the CuSi-BM<sub>60</sub> towards TC were evaluated by the CuSi-BM<sub>60</sub>/O<sub>2</sub> and CuSi-BM<sub>60</sub>/O<sub>2</sub>/Pt/carbon-PTFE system, respectively. It was concluded that 33% TC could be removed by adsorption on CuSi-BM<sub>60</sub> when the reaction time reached up to 60 min. Thus, TC adsorbed on CuSi-BM<sub>60</sub> was mainly caused by MCM-48, which may be owing to their large surface area, porous structures and surface functional groups of silica based mesoporous molecular sieves. Note that even if sparging pure O<sub>2</sub> during

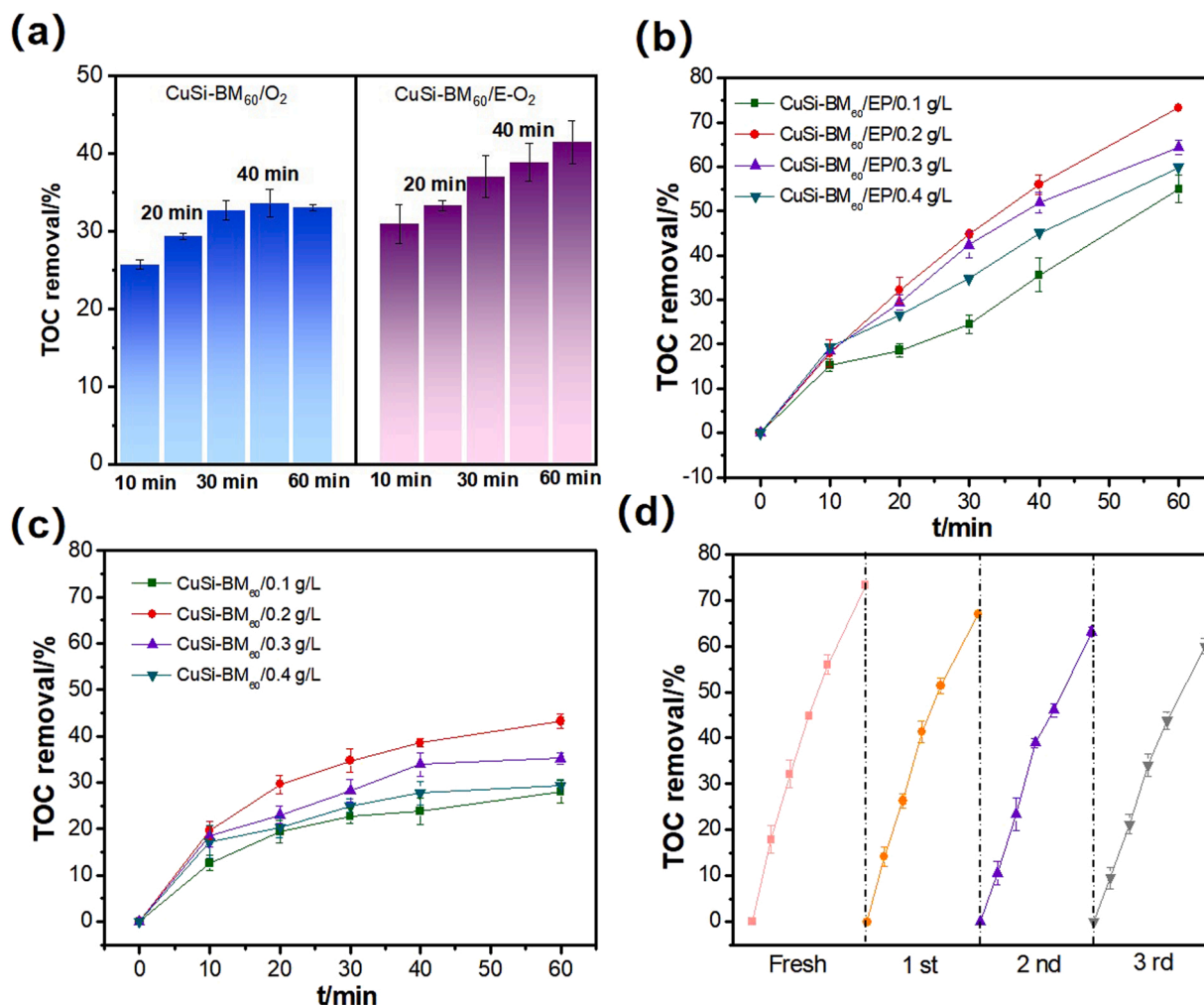
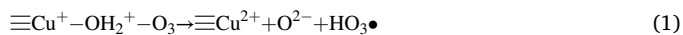


**Fig. 4.** (a) TOC degradation by CuSi-BM<sub>60</sub>/O<sub>2</sub> (left) and CuSi-BM<sub>60</sub>/O<sub>2</sub>/Pt/carbon-PTFE (right). (b) TC mineralization by different catalysts dosage in CuSi-BM<sub>60</sub>/E-peroxone. (c) TC mineralization by different catalysts dosage in CuSi-BM<sub>60</sub>/O<sub>3</sub>. (d) The recycle tests of TC mineralization in CuSi-BM<sub>60</sub>/E-peroxone. Reaction conditions: [initial TC] = 10 mg L<sup>-1</sup>; volume = 500 mL; [catalysts] = 0.2 g L<sup>-1</sup> (if used); [inlet gas phase O<sub>3</sub>] = 7.5 mg/L (if used); sparging gas flow rate = 0.25 L/min (if used); applied current = 30 mA (if used) (if used) average cell voltage = 2.3 V (if used); initial pH = 5.1.

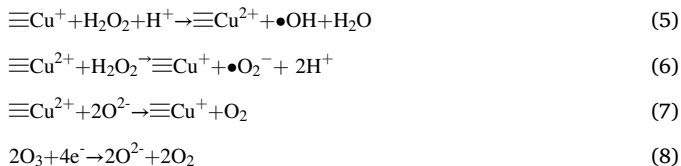
electrolysis (Pt/carbon-PTFE) could produce a certain amount of H<sub>2</sub>O<sub>2</sub> in the solution, TOC elimination was slightly (41.4%) enhanced compared with adsorption alone. Accordingly, the in-situ generated H<sub>2</sub>O<sub>2</sub> by direct electrolysis had a weak effect in the single CuSi-BM<sub>60</sub> catalytic system due to that H<sub>2</sub>O<sub>2</sub> had the low reaction rate constant with organic pollutants and CuO coupled with SiO<sub>2</sub> was hard to induce highly-efficient Fenton-like reaction to mineralize these complex contaminants. With the presence of ozone, intermediate ROSs were generated and then could degrade pollutants.

The effect of the catalyst dosage in catalytic ozonation and E-peroxone on the TC mineralization was exhibited in Fig. 4(b) and (c). When catalyst dosage increased from 0.1 to 0.2 g/L, TOC removal increased from 28% to 43.3% and 55–73.2% in CuSi-BM<sub>60</sub>/O<sub>3</sub> and CuSi-BM<sub>60</sub>/E-peroxone, respectively. Logically, the increase in CuSi-BM<sub>60</sub> dosage provided more active sites for the contact surface area between catalysts, H<sub>2</sub>O<sub>2</sub>, O<sub>3</sub> and TC, which enhanced the catalytic reaction and lead to the generation of •OH accordingly. However, reaction efficiency had no obvious increase when the dosage of CuSi-BM<sub>60</sub> was greater than 0.2 g/L in both CuSi-BM<sub>60</sub>/O<sub>3</sub> and CuSi-BM<sub>60</sub>/E-peroxone reaction. In this case, active sites were already in excess state and would cause the decrease of available reactive sites due to the agglomeration of catalysts [53]. Furthermore, the larger amount of CuSi-BM<sub>60</sub> in the liquid will hinder the collisions and interaction between free radicals and TC or corresponding intermediate products.

The experiment of CuSi-BM<sub>60</sub> for E-peroxone long-term operation was performed to evaluate the stability of catalysts and carbon-PTFE cathode in Fig. 4(d). TOC removal efficiency of TC in CuSi-BM<sub>60</sub>/E-peroxone was nearly 60% after three successive recycles of degradation testing and the concentration of the released Cu species was less than 470 µg/L at the 60 min reaction time in Fig. S11, far below the limitations of European Union directives (<2.0 mg/L) and US regulations (<1.3 mg/L). These results confirmed that good recyclability, green and low active sites loss of CuSi-BM<sub>60</sub> catalysts in the complicated advanced oxidation processes. Moreover, the potential mechanism of Cu chemical state was unveiled after CuSi-BM<sub>60</sub>/E-peroxone reaction. The valence state of Cu was analyzed via XPS (Fig. S12, Table S2) and the curve fittings results illustrated that the atomic ratio of Cu<sup>+</sup> to Cu<sup>2+</sup>/Cu<sup>+</sup> was increased from 0.303:1–0.532:1 after E-peroxone reaction. It indicated that more Cu<sup>2+</sup> ions are converted to Cu<sup>+</sup> and redox reaction of Cu<sup>2+</sup>/Cu<sup>+</sup> facilitated by higher valency of Cu species were efficient for resulting in ROSs formation and the detailed reaction route was exhibited as follows (Eqs. (1–8)).







### 3.3. Reaction mechanism of CuSi-BM<sub>60</sub>/E-peroxone process

The initial pH of aqueous solution was an important factor that influences heterogeneous CuSi-BM<sub>60</sub> based electro-peroxone treatment. As shown in Fig. 5(a), higher TOC removal efficiency of TC could be achieved as the increased pH value. Usually, high initial solution pH was beneficial to the contaminants degradation due to enhanced O<sub>3</sub> chain reaction with rich OH<sup>-</sup> (initiator of ozone decomposition). In presence of CuSi-BM<sub>60</sub> at the interface, its surface would be deprotonated (SiO-CuO<sup>-</sup>), neutral (SiO-CuOH) or protonated (SiO-CuOH<sup>+</sup>) when pH value was above, equal or below the pH<sub>pzc</sub> of Cu modified silica based mesoporous molecular sieves. As in this experiment with the presence of electro-generated H<sub>2</sub>O<sub>2</sub>, the SiO-CuOH<sup>+</sup> exhibited the best catalytic activity at pH 5.1 owing to that protonated SiO-CuOH<sup>+</sup> favored adsorption of intermediates during TC E-peroxone. Thus, the reaction distance of ROSs from heterogeneous E-peroxone and TC could be lowered. Higher pH environment inhibited the target pollutants degradation, which was attributed to that SiO-CuO<sup>-</sup> or SiO-CuOH groups had weaker electrostatic forces on the acidic intermediates at pH = 9 or pH = 7.

Previous studies revealed that the formation of metastable

Si-O-metal...HO-OH\* intermediate was the key step for mediating an interface electron-transfer process during H<sub>2</sub>O<sub>2</sub>-based AOPs. From the in-situ Raman and inserted spectroscopy (Fig. S13), it could be observed that surface peroxides generation on the interface of solid-liquid after the addition of H<sub>2</sub>O<sub>2</sub> into the CuSi-BM<sub>60</sub> slurry, which were assigned to the O-O bond in H<sub>2</sub>O<sub>2</sub>. The emerged new peak of surface-reactive complex (Si-O-metal...HO-OH\*) was conducted to identify the mediated electron-transfer mechanism in the heterogeneous E-peroxone system. In-situ LSV and EIS tests were performed to elucidate the role of ball milling enhanced interface-mediated electron transfer in Fig. 5(b) and (c). In comparison with CuSi-BM<sub>0</sub> electrode in the three-electrode system at Na<sub>2</sub>SO<sub>4</sub> solution, CuSi-BM<sub>60</sub> caused a higher onset peak, implying that the key role of ball milling contributed to improving electron transfer efficiency. When H<sub>2</sub>O<sub>2</sub> was injected into the CuSi-BM<sub>0</sub> or CuSi-BM<sub>60</sub> system, obviously enhanced in-situ LSV was observed in the catalysts-based system, suggesting that electrons could transfer from H<sub>2</sub>O<sub>2</sub> to Si-O anchored Cu via the conductive MCM-48. The current associated with CuSi-BM<sub>60</sub>/H<sub>2</sub>O<sub>2</sub> was more apparent than CuSi-BM<sub>0</sub>/H<sub>2</sub>O<sub>2</sub> systems after this combination between H<sub>2</sub>O<sub>2</sub> and ball milling treated active sites. To further probe the possible contribution of the conductivity of Cu modified catalysts in electro-generated H<sub>2</sub>O<sub>2</sub> system, EIS measurements were carried out. Nyquist plots of CuSi-BM<sub>0</sub> and CuSi-BM<sub>60</sub> based electrodes displayed that a linear portion and a typical semicircle were visible in all tested samples, which could be respectively representative of the mass transfer and charge-transfer resistances. CuSi-BM<sub>60</sub> showed much smaller semicircle radius than that of CuSi-BM<sub>0</sub>, which indicated that the charge-transfer resistance of CuSi-BM<sub>0</sub> at interface was decreased after CTAB@Cu-MCM-48 ball milling. After adding H<sub>2</sub>O<sub>2</sub>, the charge-transfer resistance further decreased and CuSi-BM<sub>60</sub>-based electrodes exhibited the strongest conductive capacity,

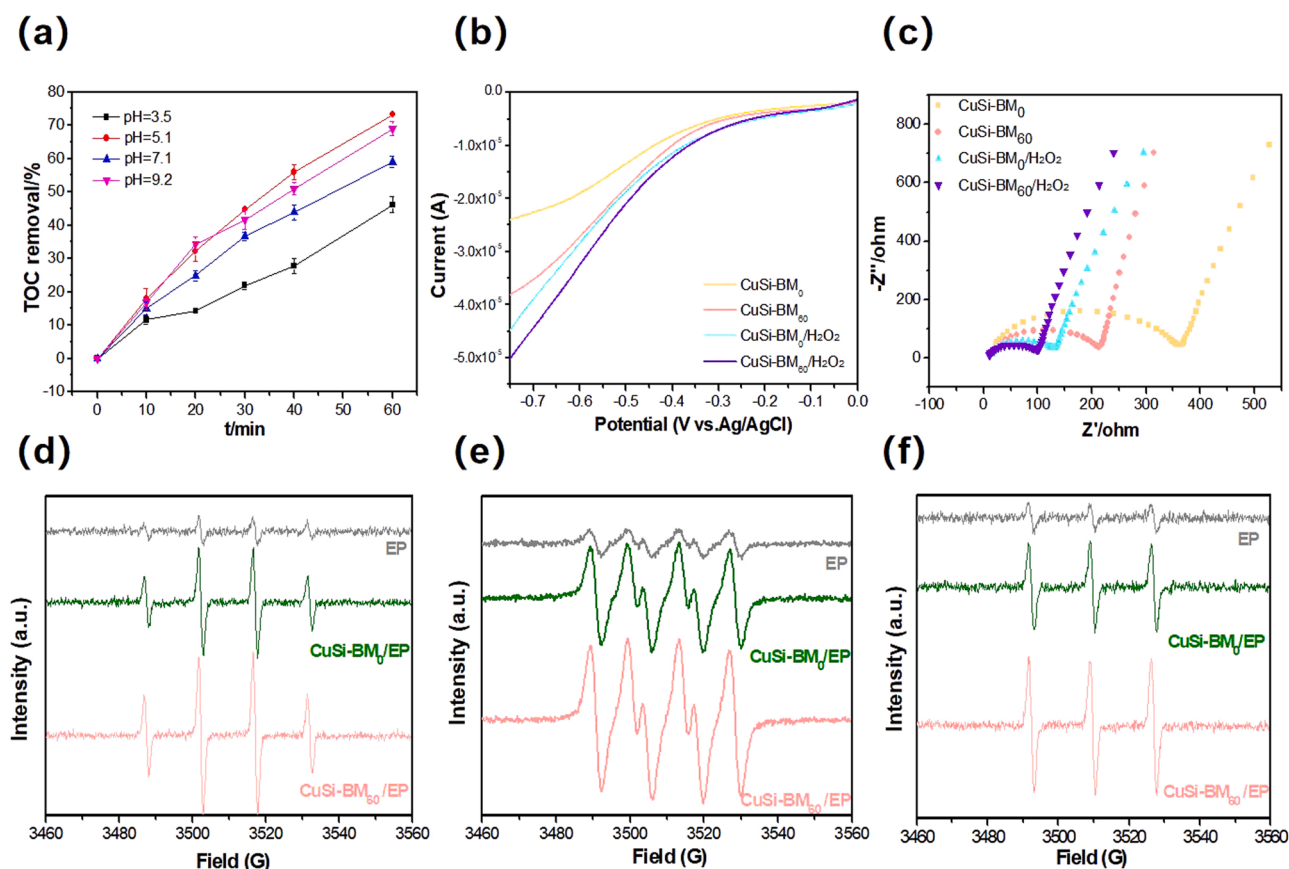
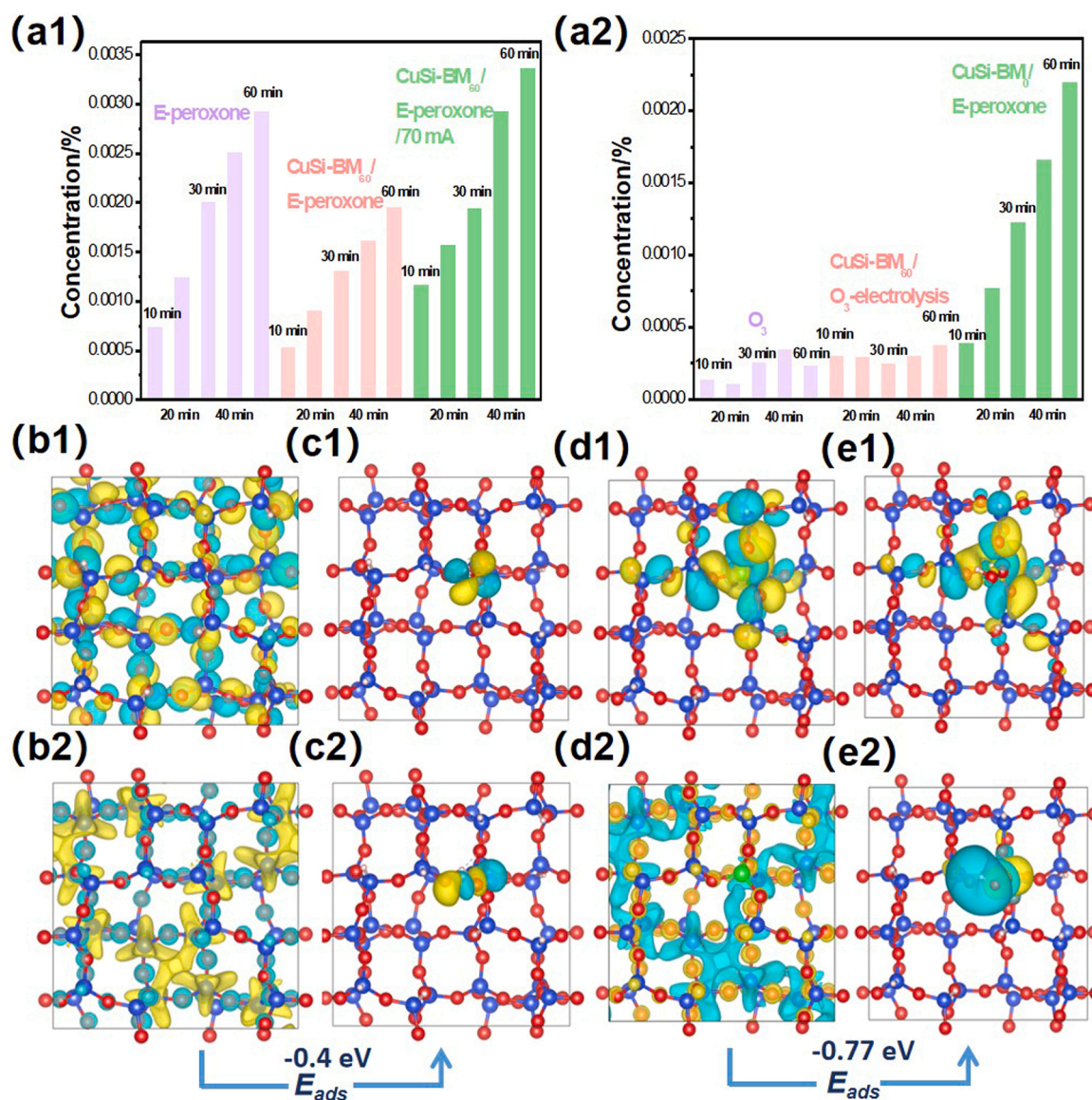


Fig. 5. (a) Influence of initial pH, (b) in-situ LSV, (c) in-situ EIS, (d) •OH, (e) O<sub>2</sub>•<sup>-</sup> and (f) <sup>1</sup>O<sub>2</sub> EPR spectra in different reaction systems. Reaction conditions: [initial TC] = 10 mg L<sup>-1</sup>; volume = 500 mL; [catalysts] = 0.2 g L<sup>-1</sup> (if used) (if used); [inlet gas phase O<sub>3</sub>] = 7.5 mg/L (if used); sparging gas flow rate = 0.25 L/min (if used); applied current = 30 mA (if used); average cell voltage = 2.3 V.

which was in accordance with the results of in-situ LSV. This manifested the resulted CuSi-BM<sub>60</sub> accelerated the electron transfer and the complex of H<sub>2</sub>O<sub>2</sub> with CuSi-BM<sub>60</sub> thus improved the performance of catalysts during E-peroxone reaction. EPR was employed using different trapping agent to examine ROSs in catalytic processes, which was depicted in Fig. 5(d–f). The weak signal of DMPO-•OH (four lines, 1:2:2:1) was captured in the single E-peroxone process, proving the existence of •OH from the peroxide reaction between ozone and electro-generated H<sub>2</sub>O<sub>2</sub>. It could be observed that the presence of catalysts would enhance the generation of •OH and the signal of DMPO-•OH adduct in the CuSi-BM<sub>60</sub>/E-peroxone system was higher than that of the CuSi-BM<sub>0</sub>/E-peroxone system. Similarly, the EPR signals of DMPO-O<sub>2</sub>•<sup>-</sup> and TEMP-O<sub>2</sub> (1:1:1 triplet signals) adducts became stronger when active sites were modified by ball milling treatment. These results confirm that enhanced ROSs generation resulted from the high valency state of CuSi-BM<sub>60</sub> after ball milling were primarily responsible for the TC degradation and mineralization during E-peroxone.

### 3.4. DFT calculation and ROSs generation pathway

The concentration variation of electro-generated H<sub>2</sub>O<sub>2</sub> during E-peroxone and CuSi-BM<sub>60</sub>/E-peroxone was displayed in Fig. 6(a). Lower concentration of H<sub>2</sub>O<sub>2</sub> was detected in the heterogeneous E-peroxone process due to the unique interface interaction between solid and liquid phase. Higher initial current intensity would enhance the H<sub>2</sub>O<sub>2</sub> generation in the 70 mA, which was in accordance with the results of Fig. 3. Meanwhile, there was barely H<sub>2</sub>O<sub>2</sub> in O<sub>3</sub> system due to the mild generation efficiency in the only O<sub>3</sub> chain reaction. CuSi-BM<sub>60</sub>/O<sub>3</sub>-electrolysis process was also hardly to generate in-situ electro-generated H<sub>2</sub>O<sub>2</sub>, which was the key reason for lower TC mineralization and degradation than CuSi-BM<sub>60</sub>/E-peroxone. To understand the crucial role of electro-generated H<sub>2</sub>O<sub>2</sub> and active sites of CuSi-BM<sub>60</sub> in the chemisorption process, the chemical process were investigated by DFT modeling to provide insights into the key reaction mechanisms. The adsorption energy (*E*<sub>ads</sub>) of H<sub>2</sub>O<sub>2</sub> on atoms of different clusters was determined from  $E_{\text{ads}} = E_{\text{H}_2\text{O}_2+\text{Si}} - (E_{\text{Si}} + E_{\text{H}_2\text{O}_2})$  and  $E_{\text{ads}} = E_{\text{H}_2\text{O}_2+\text{Cu}} - (E_{\text{Cu}} + E_{\text{H}_2\text{O}_2})$ , where  $E_{\text{H}_2\text{O}_2+\text{Si}}$  and  $E_{\text{H}_2\text{O}_2+\text{Cu}}$  were the total energy of



**Fig. 6.** (a1, a2) The concentration variation of electro-generated H<sub>2</sub>O<sub>2</sub> during different systems. (b1) HOMO and (b2) LUMO patterns of optimized configurations of the Si–O–Si cluster. (c1) HOMO and (c2) LUMO patterns of optimized configurations of the Si–O–Si cluster adsorbed by H<sub>2</sub>O<sub>2</sub>. (d1) HOMO and (d2) LUMO patterns of optimized configurations of the Cu–O–Si cluster. (e1) HOMO and (e2) LUMO patterns of optimized configurations of the Cu–O–Si cluster adsorbed by H<sub>2</sub>O<sub>2</sub>. The red, blue, green and salmon pink spheres are O, Si, Cu, H, respectively. *E*<sub>ads</sub> represented the adsorption energy of optimized configurations adsorbed by H<sub>2</sub>O<sub>2</sub>.

the Si and Cu atom in Si–O–Si...HO–OH\* and Si–O–Cu...HO–OH\* clusters with H<sub>2</sub>O<sub>2</sub> adsorption, respectively.  $E_{H_2O_2}$ ,  $E_{Si}$  and  $E_{Cu}$  were respectively the total energies of an isolated H<sub>2</sub>O<sub>2</sub> molecule, Si–O–Si and Cu...O–Si clusters. The negative Eads values of H<sub>2</sub>O<sub>2</sub> adsorption on Si and Cu atoms facets in Si–O–Si and Cu...O–Si clusters were –0.4 and –0.77 eV, which indicated that the interaction between H<sub>2</sub>O<sub>2</sub> and CuSi-BM<sub>60</sub> reaction could proceed spontaneously and H<sub>2</sub>O<sub>2</sub> tended to locate at the Cu atoms of CuSi-BM<sub>60</sub> for further decomposition and activation, thus favoring the electron transfer from the active sites of the CuSi-BM<sub>60</sub> to H<sub>2</sub>O<sub>2</sub> as proved by the larger adsorption energy according to Fig. 6(b)–(e) and Fig. S14 for the free H<sub>2</sub>O<sub>2</sub>. The gap between highest occupied molecular orbital (HOMO) and lowest unoccupied molecular orbital (LUMO) gap of clusters reflected the chemical reactivity and kinetic stability of different catalysts [54]. Molecular orbital gap pattern of all structures was exhibited in Fig. S15–S18. The introduction of Cu atom into carriers decreased the HOMO–LUMO energy level gap from 5.987 (pure Si–O clusters) to 4.741 eV, implying that Cu as active sites for enhancing catalytic efficiency was reasonable and feasible in Fig. 7(a). After H<sub>2</sub>O<sub>2</sub> was absorbed to the surface of atoms in clusters, the lower energy gap for Si–O...Cu...HO–OH\* (3.545 eV) than Si–O–Si...HO–OH\* (4.424 eV) could be observed. Therefore, these results implied that the complex between CuSi-BM<sub>60</sub> and H<sub>2</sub>O<sub>2</sub> had significantly higher chemical reactivity than pure MCM-48 clusters owing to accelerated electron transfer, which was the initiator of ozone decomposition for E-peroxone reaction. The charge density analysis evidenced that enhanced electron transfer after the presence of Cu and H<sub>2</sub>O<sub>2</sub> complex occurred according to the uneven HOMO and LUMO electron cloud interaction, which corresponded well to the results derived from in-situ LSV and EIS. In Fig. 7(b) and (c), the anchored Cu by Si–O obviously lowered the intensity of density of states (DOS) of Si–O clusters below the Fermi level owing to

the transfer of electron from Cu to silicon skeleton [55]. After H<sub>2</sub>O<sub>2</sub> complexing, the DOS was shifted to higher energy level under electron-withdrawing effect, corresponding to the transfer of electron to absorbed H<sub>2</sub>O<sub>2</sub> and it would lead to interface complex decomposition and generate more ROSSs. However, DOS of Si–O cluster did not change after H<sub>2</sub>O<sub>2</sub>'s adsorption, indicating that pure silicon was non-reactive with H<sub>2</sub>O<sub>2</sub>.

Additionally, after H<sub>2</sub>O<sub>2</sub> adsorption onto Cu atom in the models of Si–O–Cu...HO–OH\* clusters, the O–O bond length ( $l_{O-O}$ ) was shortened from 1.468 Å to 1.42 Å, indicating that the O–O bond of H<sub>2</sub>O<sub>2</sub> molecules was hard to be directly activated and ready to be cleaved to generate ROSSs by chemical oxidizing agent in this catalytic system. Hence, rather than O–O bond in H<sub>2</sub>O<sub>2</sub> molecule, the O–H bond of adsorbed H<sub>2</sub>O<sub>2</sub> on the side of Cu atom Si–O...Cu...HO–OH\* was probably the sites where the interface generated complex was decomposed and ready to be cleaved to generate HO<sub>2</sub>•/O<sub>2</sub>•<sup>–</sup> radicals. In view of enhanced Eads of H<sub>2</sub>O<sub>2</sub> molecule and metal atom in the framework of Si–O–Si, the O–H<sub>1</sub> bond length ( $l_{O-H1}$ ) near Si–O–Si or Cu...O–Si clusters and the O–H<sub>2</sub> bond length ( $l_{O-H2}$ ) far away from Si–O–Si or Cu...O–Si clusters were calculated according to the results of Fig. 7(d), 7(e) and Table S3. When H<sub>2</sub>O<sub>2</sub> was adsorbed on the different clusters, the  $l_{O-H2}$  in H<sub>2</sub>O<sub>2</sub> remained still unchanged (0.976 Å for Si–O...Cu...HO–OH\*, 0.981 Å for Si–O–Si...HO–OH\*, 0.98 Å for free H<sub>2</sub>O<sub>2</sub>). Nevertheless, the bond of  $l_{O-H1}$  (1.00 Å) on the Si–O...Cu...HO–OH\* clusters was stretched appreciably compared to that in free H<sub>2</sub>O<sub>2</sub> (0.979 Å) and Si–O–Si clusters (0.98 Å), indicative of the activation of H<sub>2</sub>O<sub>2</sub> on the O–H<sub>1</sub> bond. Based on the electron transfer from the Cu atom to H<sub>2</sub>O<sub>2</sub> and the prolonged  $l_{O-O}$ , the analysis of bond angle ( $\angle$ ) before and after complexing on the different structure sought to be investigated. Computational studies revealed that the  $\angle_{O-O-H1}$  or  $\angle_{O-O-H2}$  in free H<sub>2</sub>O<sub>2</sub> was approximately 99.98°. The Cu modified

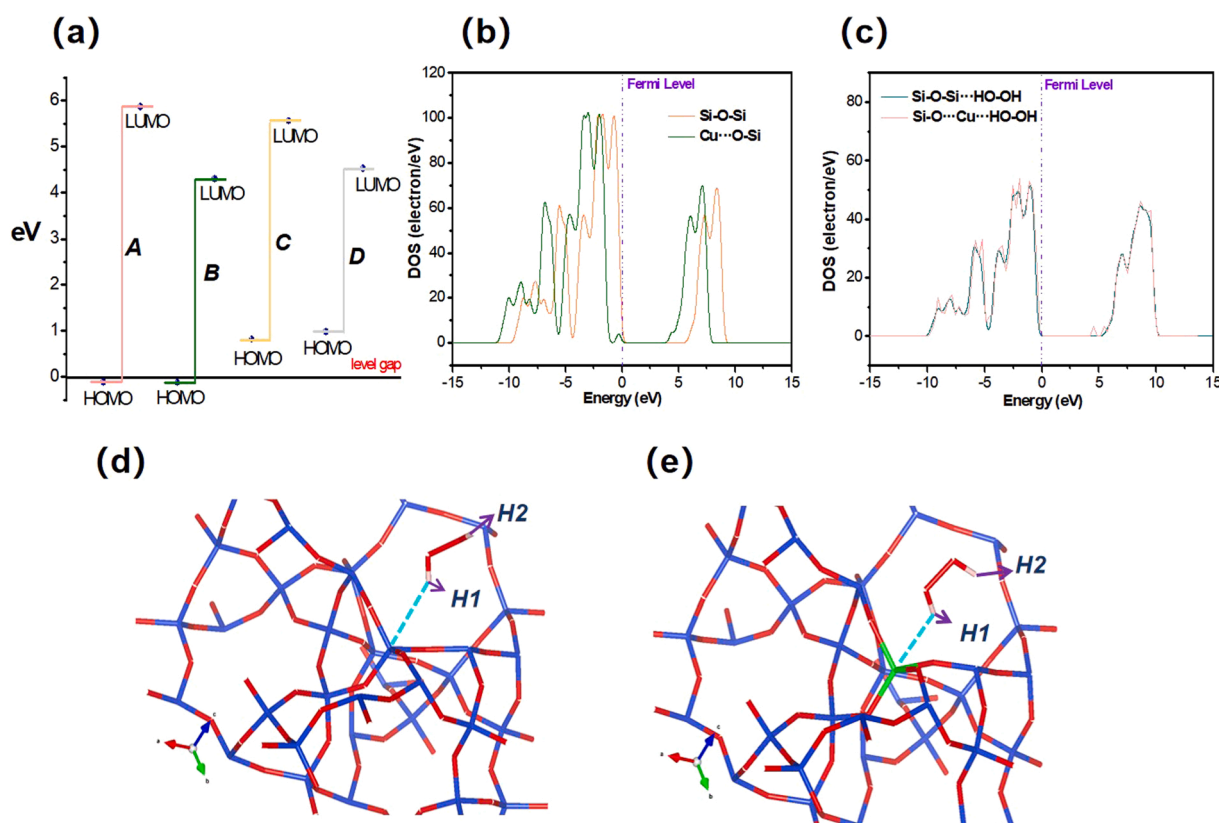


**Fig. 7.** (a) The computed HOMO–LUMO energy value of different clusters (A, B, C and D represent the Si–O–Si, Si–O–Si...HO–OH\*, Cu...O–Si and Si–O...Cu...HO–OH\*). (b) DOS of Si–O–Si and Cu modified Si–O clusters. (c) DOS of Si–O–Si and Cu modified Si–O clusters adsorbed by H<sub>2</sub>O<sub>2</sub> (d) The Si–O–Si stick style adsorbed by H<sub>2</sub>O<sub>2</sub>. (e) The Cu...O–Si stick style adsorbed by H<sub>2</sub>O<sub>2</sub>. The red, blue, green and salmon pink line are O, Si, Cu, H, respectively. (For interpretation of the references to color in this figure legend, the reader is referred to the web version of this article.)



Si–O–Si clusters system demonstrated a larger  $\angle_{\text{O–O–H1}}$  ( $110.20^\circ$ ) and  $\angle_{\text{O–O–H2}}$  ( $105.96^\circ$ ), in contrast with Si–O–Si...HO–OH\* cluster with  $\angle_{\text{O–O–H1}}$  ( $99.93^\circ$ ) and  $\angle_{\text{O–O–H2}}$  ( $100.32^\circ$ ). The maximum  $\angle_{\text{O–O–H1}}$  of  $\text{H}_2\text{O}_2$  near to the Cu atom in Si–O–Si clusters indicated that it was desirable for activating  $\text{H}_2\text{O}_2$  into free radicals via the cleavage of the O–H1 bond, which agreed well with the variation of bond length. The above DFT calculations clearly identified that although the presence of Si–O–Si anchored CuO complex with  $\text{H}_2\text{O}_2$  can enhance  $\text{H}_2\text{O}_2$  activation and in the circumstances, it was more likely to serve as the active site for  $\text{O}_3$  attacking.

DFT calculations are also performed to verify this the interaction among  $\text{O}_3$ ,  $\text{H}_2\text{O}_2$  and active sites to reveal the reaction route of ROSs generation (Fig. S19). The stable adsorption of  $\text{H}_2\text{O}_2$  on the CuSi-BM<sub>60</sub> could lead to the form of the Si–O...Cu...O–OH\* complex by spontaneously releasing one proton owing to increase in E value of clusters in the adsorption process [12]. Then an endothermal reaction (reaction A) could be observed in the process of Si–O...Cu...O–OH\* decomposition into  $\text{HO}_2\bullet$  and Si–O...Cu, which was not a feasible process owing to the positive  $\Delta E = 0.669$ . However, the presence of  $\text{O}_3$  would help to break the Si–O...Cu...O–OH\* complex. Actually, the reaction B could verify this and an obvious exothermal reaction might be achieved by the breaking of Si–O...Cu...O–OH\* complex after  $\text{O}_3$  addition to generate  $\text{O}_3\bullet^-$ ,  $\text{HO}_2\bullet$  and Si–O...Cu. The energy release of 3.496 eV suggested that the decomposition of the Si–O...Cu...O–OH\* complex would proceed much more easily with the presence of  $\text{O}_3$ . Therefore, the catalytic mechanism of E-peroxone on the interface could be proposed, which was different from the homogeneous peroxone reaction (Fig. S20). The in situ electro-generated  $\text{H}_2\text{O}_2$  could adsorb to the Si–O...Cu active site and the produced Si–O...Cu...HO–OH\* species would generate Si–O...Cu...O–OH\* and  $\text{H}^+$ . Then  $\text{O}_3$  molecule would attack the complex compound to form  $\text{HO}_2\bullet/\text{O}_3\bullet^-$  and stimulate the ROSs chain reaction. In one pathway,  $\text{O}_3\bullet^-$  would combine with  $\text{H}_2\text{O}$  to form  $\text{HO}_3\bullet$ , which quickly transferred into  $\text{O}_2\bullet^-$  and  $\bullet\text{OH}$ . In another one,  $\text{HO}_2\bullet$  would can act as a radical initiator in the oxidation system to induce a series of ROSs chain reactions and it could convert to  $\text{H}^+$  and  $\text{O}_2\bullet^-$ . The produced  $\text{O}_2\bullet^-$  would also react with to generate  $\text{O}_2$  and  $\text{O}_3\bullet^-$ . As the nonradical species,  $^1\text{O}_2$  with a mild oxidation potential has been considered as playing an important role in the radical-based oxidations.  $^1\text{O}_2$  can also be formed by the reactions via electron transfer between the surface- $\text{O}_3$  complex owing to the adsorption between  $\text{O}_3$  molecules and active sites. Meanwhile,  $\text{O}_2\bullet^-$  from the dissociation products of  $\text{O}_3$  on the active sites would lead to the evolution of  $^1\text{O}_2$  by the reaction with  $\bullet\text{OH}$  or  $\text{HO}_2\bullet$ .

### 3.5. Intermediate products and degradation pathway

Fig. S21 exhibited the pH variation in E-peroxone and CuSi-BM<sub>60</sub>/E-peroxone processes. Similar phenomenon could be observed that pH significantly decreased at first 10 or 20 min. At this stage, TC might quickly decompose owing to high reaction rate of ozone and ROSs, producing many intermediates and small carboxylic acid. The pH value of single E-peroxone process decreased faster than that of CuSi-BM<sub>60</sub>/E-peroxone, which suggested that more oxalic acid or acetic acid were accumulated. At 60 min oxidation time, compared to E-peroxone, CuSi-BM<sub>60</sub>/E-peroxone has higher pH value owing to more efficient mineralization of intermediate products by the generated  $\bullet\text{OH}$  with the reaction rate constants in the order of  $10^6$ – $10^9 \text{ L M}^{-1} \text{ s}^{-1}$ .

Figs. S22 and S23 showed the extracted ion chromatography of TC and all intermediate in E-peroxone and CuSi-BM<sub>60</sub>/E-peroxone, respectively. The peak of TC at  $m/z$  445.16 and corresponding retention time was 3.7 s by UPLC/MS/MS analysis. Nine kinds of intermediates in E-peroxone could be observed and the proposed degradation pathway were presented in Fig. 8(a). In one pathway, P-457.12 formed via loss of N-methyl groups on amine site due to the low N–C bond energy, introduction of hydrogen on electron-withdrawing C–C double bond and hydroxyl groups, which was similar with the intermediate product with  $m/z$  of 435 reported by Cao et al. [56]. Then the dehydroxylation process would occur and generate P-416.09 from the decomposition of P-457.12. Additionally, P-461.15, P-416.16, P-477.15 and P-493.14 were the frequent intermediates during TC ozonation, which were formed by hydroxylation, dehydroxylation, N-dealkylation and addition of O atom [57]. Based on the loss of hydroxyl, amide and intramolecular condensation, P-374.12 subsequently would generate via the further oxidation. In the system of CuSi-BM<sub>60</sub>/E-peroxone, less intermediate products could be detected due to the higher catalytic efficiency in Fig. 8 (b). The reaction route was still including hydroxylation and N-dealkylation after attacking successively by  $\text{O}_3$  or other ROSs.

### 4. Conclusion

This work would extend the application of confined Cu nanorod anchored by Si–O via green ball milling technology as efficient catalysts, which was coupled with E-peroxone process in solving increasingly serious water pollution problems. With the high valency of Cu species generation in the framework of Si–O skeleton of MCM-48 by ball milling, the resultant CuSi-BM<sub>60</sub> delivered excellent E-peroxone catalytic performance in ROSs generation and mass transfer for organic pollutant degradation, as evidenced by the significantly higher TOC removal of TC

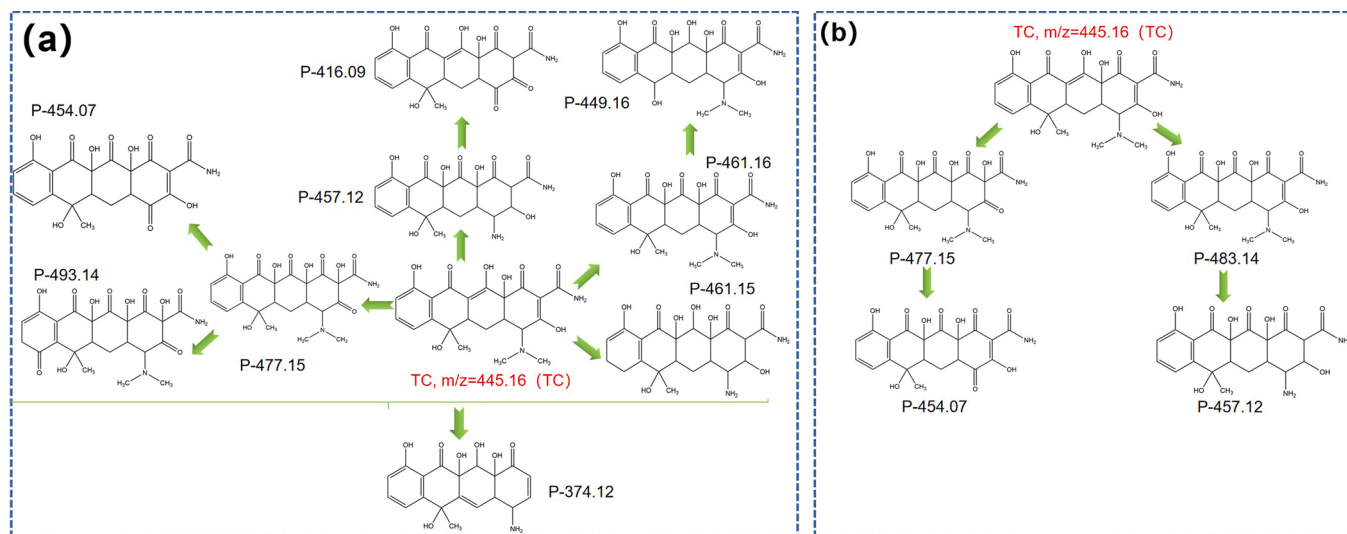


Fig. 8. Reaction pathway of TC in (a) E-peroxone and (b) CuSi-BM<sub>60</sub>/E-peroxone.

than that of the control sample (E-peroxone alone or CuSi-BM<sub>60</sub>/E-peroxone) and efficient H<sub>2</sub>O<sub>2</sub> utilization. Meanwhile, the longer I<sub>O-H1</sub> bond length, wider ∠O-O-H1 bond angle near from Cu atom suggested that the interface complex Si-O...Cu...HO-OH\* cluster with lower HOMO-LUMO energy level gap was more active than around Si atom for both H<sub>2</sub>O<sub>2</sub> adsorption and decomposition. Furthermore, lower adsorption energy (E<sub>ads</sub>) and enhanced electron transfer on the bond bridge was achieved by the construction of Cu modified silicon skeleton. The uneven electron cloud distribution could serve as electron shuttle during electro-generated H<sub>2</sub>O<sub>2</sub> decomposition, accelerating the electron transfer from H<sub>2</sub>O<sub>2</sub> onto the surface of catalysts. Benefiting from the admirable catalytic activity and interface electron transfer capacity (electro-generated H<sub>2</sub>O<sub>2</sub>→Cu clusters→Si network), the CuSi-BM<sub>60</sub> could have significant application potential in the E-peroxone-mediated remediation of contaminated aqueous.

#### CRedit authorship contribution statement

**Shangyi Li:** Methodology, Investigation, Writing – original draft, Data validation. **Yujue Wang and Jun Huang:** Supervision, Funding acquisition, Writing – review & editing. **Gang Yu:** Supervision.

#### Declaration of Competing Interest

The authors declare that they have no known competing financial interests or personal relationships that could have appeared to influence the work reported in this paper.

#### Acknowledgements

This work was financially supported by the project of China Postdoctoral Science Foundation (2020TQ0165), China Postdoctoral Science Foundation (2021M691768), the National Key Research and Development Program of China 2018YFC1803100 and 2019YFC1805601.

#### Appendix A. Supporting information

Supplementary data associated with this article can be found in the online version at doi:10.1016/j.apcatb.2021.120930.

#### References

- [1] G.G. Wang, S.H. Zhou, X.K. Han, L.L. Zhang, S.Y. Ding, Y. Li, D.J. Zhang, K. Zarin, Occurrence, distribution, and source track of antibiotics and antibiotic resistance genes in the main rivers of Chongqing city, southwest China, *J. Hazard. Mater.* 389 (2020).
- [2] P. Kovalakova, L. Cizmas, T.J. McDonald, B. Marsalek, M.B. Feng, V.K. Sharma, Occurrence and toxicity of antibiotics in the aquatic environment: a review, *Chemosphere* 251 (2020).
- [3] W.J. Andrews, J.R. Masoner, I.M. Cozzarelli, Emerging contaminants at a closed and an operating landfill in Oklahoma, *Ground Water Monit. Remediat.* 32 (2012) 120–130.
- [4] O. Cardoso, J.M. Porcher, W. Sanchez, Factory-discharged pharmaceuticals could be a relevant source of aquatic environment contamination: review of evidence and need for knowledge, *Chemosphere* 115 (2014) 20–30.
- [5] X. Zhou, Z. Zeng, G. Zeng, C. Lai, R. Xiao, S. Liu, D. Huang, L. Qin, X. Liu, B. Li, H. Yi, Y. Fu, L. Li, Z. Wang, Persulfate activation by swine bone char-derived hierarchical porous carbon: multiple mechanism system for organic pollutant degradation in aqueous media, *Chem. Eng. J.* 383 (2020).
- [6] K. Li, A. Yediler, M. Yang, S. Schulte-Hostede, M.H. Wong, Ozonation of oxytetracycline and toxicological assessment of its oxidation by-products, *Chemosphere* 72 (2008) 473–478.
- [7] R.P. Schwarzenbach, B.I. Escher, K. Fenner, T.B. Hofstetter, C.A. Johnson, U. Von Gunten, B. Wehrli, The challenge of micropollutants in aquatic systems, *Science* 313 (2006) 1072–1077.
- [8] B.I. Escher, H.M. Stapleton, E.L. Schymanski, Tracking complex mixtures of chemicals in our changing environment, *Science* 367 (2020) 388.
- [9] X. Fan, J. Gao, W. Li, J. Huang, G. Yu, Determination of 27 pharmaceuticals and personal care products (PPCPs) in water: the benefit of isotope dilution, *Front. Environ. Sci. Eng.* 14 (2020).
- [10] X. Jiang, Y. Qu, M. Zhong, W. Li, J. Huang, H. Yang, G. Yu, Seasonal and spatial variations of pharmaceuticals and personal care products occurrence and human health risk in drinking water - a case study of China, *Sci. Total Environ.* 694 (2019).
- [11] W. Chen, J. Xie, X. Li, L. Li, Oxygen vacancies and Lewis sites activating O-3/H<sub>2</sub>O<sub>2</sub> at wide pH range via surface electron transfer over CeOx@SiO<sub>2</sub> for nitrobenzene mineralization, *J. Hazard. Mater.* 406 (2021).
- [12] Z. Guo, Y. Xie, J. Xiao, Z.-J. Zhao, Y. Wang, Z. Xu, Y. Zhang, L. Yin, H. Cao, J. Gong, Single-atom Mn-N-4 site-catalyzed peroxone reaction for the efficient production of hydroxyl radicals in an acidic solution, *J. Am. Chem. Soc.* 141 (2019) 12005–12010.
- [13] Z.D. Ristovski, L. Morawska, N.D. Bofinger, J. Hitchins, Submicrometer and supermicrometer particulate emission from spark ignition vehicles, *Environ. Sci. Technol.* 32 (1998) 3845–3852.
- [14] S. Li, J. Huang, X. Li, L. Li, The relation of interface electron transfer and PMS activation by the H-bonding interaction between composite metal and MCM-48 during sulfamethazine ozonation, *Chem. Eng. J.* 398 (2020).
- [15] Y. Xu, Y. Wu, W. Zhang, X. Fan, Y. Wang, H. Zhang, Performance of artificial sweetener sucralose mineralization via UV/O-3 process: kinetics, toxicity and intermediates, *Chem. Eng. J.* 353 (2018) 626–634.
- [16] H. Wang, B. Bakheet, S. Yuan, X. Li, G. Yu, S. Murayama, Y. Wang, Kinetics and energy efficiency for the degradation of 1,4-dioxane by electro-peroxone process, *J. Hazard. Mater.* 294 (2015) 90–98.
- [17] Y. Wang, G. Yu, S. Deng, J. Huang, B. Wang, The electro-peroxone process for the abatement of emerging contaminants: mechanisms, recent advances, and prospects, *Chemosphere* 208 (2018) 640–654.
- [18] S. Yuan, Z. Li, Y. Wang, Effective degradation of methylene blue by a novel electrochemically driven process, *Electrochim. Commun.* 29 (2013) 48–51.
- [19] C. Von Sonntag, U. Von Gunten, Chemistry of Ozone in Water and Wastewater Treatment: From Basic Principles to Applications, 2012.
- [20] Y. Li, W. Shen, S. Fu, H. Yang, G. Yu, Y. Wang, Inhibition of bromate formation during drinking water treatment by adapting ozonation to electro-peroxone process, *Chem. Eng. J.* 264 (2015) 322–328.
- [21] B. Bakheet, S. Yuan, Z. Li, H. Wang, J. Zuo, S. Komarneni, Y. Wang, Electro-peroxone treatment of Orange II dye wastewater, *Water Res.* 47 (2013) 6234–6243.
- [22] Z. Li, S. Yuan, C. Qiu, Y. Wang, X. Pan, J. Wang, C. Wang, J. Zuo, Effective degradation of refractory organic pollutants in landfill leachate by electro-peroxone treatment, *Electrochim. Acta* 102 (2013) 174–182.
- [23] A. Fischbacher, J. Sonntag, C.V. Sonntag, T. C. The OH radical yield in the H<sub>2</sub>O<sub>2</sub> + O<sub>3</sub> (peroxone) reaction, *Environ. Sci.* 47 (2013) 9959–9964.
- [24] D. Wu, G. Lu, J. Yao, C. Zhou, F. Liu, J. Liu, Adsorption and catalytic electro-peroxone degradation of fluconazole by magnetic copper ferrite/carbon nanotubes, *Chem. Eng. J.* 370 (2019) 409–419.
- [25] X. Li, W. Chen, Y. Tang, L. Li, Relationship between the structure of Fe-MCM-48 and its activity in catalytic ozonation for diclofenac mineralization, *Chemosphere* 206 (2018) 615–621.
- [26] S. Li, Y. Tang, W. Chen, Z. Hu, X. Li, L. Li, Heterogeneous catalytic ozonation of clofibric acid using Ce/MCM-48: preparation, reaction mechanism, comparison with Ce/MCM-41, *J. Colloid Interface Sci.* 504 (2017) 238–246.
- [27] W. Li, X. Lu, K. Xu, J. Qu, Z. Qiang, Cerium incorporated MCM-48 (Ce-MCM-48) as a catalyst to inhibit bromate formation during ozonation of bromide-containing water: efficacy and mechanism, *Water Res.* 86 (2015) 2–8.
- [28] L. Wang, L. Xing, J. Liu, T. Qi, S. Zhang, Y. Ma, P. Ning, Construction of lattice-confined Co-MCM-48 for boosting sulfite oxidation in wet desulfuration, *Chem. Eng. J.* 407 (2021).
- [29] S. Li, J. Wang, Y. Ye, Y. Tang, X. Li, F. Gu, L. Li, Composite Si-O-metal network catalysts with uneven electron distribution: enhanced activity and electron transfer for catalytic ozonation of carbamazepine, *Appl. Catal. B Environ.* 263 (2020).
- [30] S. Gil, J.M. Garcia-Vargas, L.F. Liotta, G. Pantaleo, M. Ousmane, L. Retailleau, A. Giroir-Fendler, Catalytic oxidation of propene over Pd catalysts supported on CeO<sub>2</sub>, TiO<sub>2</sub>, Al<sub>2</sub>O<sub>3</sub> and M/Al<sub>2</sub>O<sub>3</sub> oxides (M = Ce, Ti, Fe, Mn), *Catalysts* 5 (2015) 671–689.
- [31] S. Li, X. Li, H. Wu, X. Sun, F. Gu, L. Zhang, H. He, L. Li, Mechanism of synergistic effect on electron transfer over Co-Ce/MCM-48 during ozonation of pharmaceuticals in water, *ACS Appl. Mater. Interfaces* 11 (2019) 23957–23971.
- [32] W. Chen, X. Li, Y. Tang, J. Zhou, D. Wu, Y. Wu, L. Li, Mechanism insight of pollutant degradation and bromate inhibition by Fe-Cu-MCM-41 catalyzed ozonation, *J. Hazard. Mater.* 346 (2018) 226–233.
- [33] Q. Sun, L. Li, H. Yan, X. Hong, K.S. Hui, Z. Pan, Influence of the surface hydroxyl groups of MnOx/SBA-15 on heterogeneous catalytic ozonation of oxalic acid, *Chem. Eng. J.* 242 (2014) 348–356.
- [34] S.M. Vickers, R. Gholami, K.J. Smith, M.J. MacLachlan, Mesoporous Mn- and La-doped cerium oxide/cobalt oxide mixed metal catalysts for methane oxidation, *ACS Appl. Mater. Interfaces* 7 (2015) 11460–11466.
- [35] K. Ralphs, C. Hardacre, S.L. James, Application of heterogeneous catalysts prepared by mechanochemical synthesis, *Chem. Soc. Rev.* 42 (2013) 7701–7718.
- [36] Y. Yang, S. Zhang, S. Wang, K. Zhang, H. Wang, J. Huang, S. Deng, B. Wang, Y. Wang, G. Yu, Ball milling synthesized MnOx as highly active catalyst for gaseous POPs removal: significance of mechanochemically induced oxygen vacancies, *Environ. Sci. Technol.* 49 (2015) 4473–4480.
- [37] D. Ruyter, G. Chamoulaud, D. Belanger, L. Roue, Electrocatalytic reduction of nitrate on copper electrodes prepared by high-energy ball milling, *J. Electroanal. Chem.* 596 (2006) 13–24.
- [38] S. Deng, L. Liu, G. Cagnetta, J. Huang, G. Yu, Mechanochemically synthesized S-ZVI(bm) composites for the activation of persulfate in the pH-independent degradation of atrazine: Effects of sulfur dose and ball-milling conditions, *Chem. Eng. J.* 423 (2021).
- [39] M.M. Barroso Quiroga, B.P. Barbero, L.E. Cadus, Synthesis of a catalyst of Mn-Fe-O by mechano-chemical reaction, *Appl. Catal. A Gen.* 474 (2014) 26–33.

- [40] E. Martinez-Carballo, C. Gonzalez-Barreiro, S. Scharf, O. Gans, Environmental monitoring study of selected veterinary antibiotics in animal manure and soils in Austria, *Environ. Pollut.* 148 (2007) 570–579.
- [41] D.G.J. Larsson, C. de Pedro, N. Paxeus, Effluent from drug manufactures contains extremely high levels of pharmaceuticals, *J. Hazard. Mater.* 148 (2007) 751–755.
- [42] R.M. Sellers, Spectrophotometric determination of hydrogen-peroxide using potassium titanium(IV) oxalate, *Analyst* 105 (1980) 950–954.
- [43] N. Milan-Segovia, Y. Wang, F.S. Cannon, R.C. Voigt, J.C. Furness Jr., Comparison of hydroxyl radical generation for various advanced oxidation combinations as applied to foundries, *Ozone Sci. Eng.* 29 (2007) 461–471.
- [44] J. Liu, L. Wang, N. Wang, F. Guo, L. Hou, Y. Chen, J. Liu, Y. Zhao, L. Jiang, A. Robust, Cu(OH)(2) nanoneedles mesh with tunable wettability for nonaqueous multiphase liquid separation, *Small* 13 (2017).
- [45] F. Lin, Z. Wang, Z. Zhang, L. Xiang, D. Yuan, B. Yan, Z. Wang, G. Chen, Comparative investigation on chlorobenzene oxidation by oxygen and ozone over a MnO<sub>x</sub>/Al<sub>2</sub>O<sub>3</sub> catalyst in the presence of SO<sub>2</sub>, *Environ. Sci. Technol.* 55 (2021) 3341–3351.
- [46] Y. Pu, Y. Luo, X. Wei, J. Sun, L. Li, W. Zou, L. Dong, Synergistic effects of Cu<sub>2</sub>O-decorated CeO<sub>2</sub> on photocatalytic CO<sub>2</sub> reduction: surface Lewis acid/base and oxygen defect, *Appl. Catal. B Environ.* 254 (2019) 580–586.
- [47] H. Mai, D. Zhang, L. Shi, T. Yan, H. Li, Highly active Ce<sub>1-x</sub>Cu<sub>x</sub>O<sub>2</sub> nanocomposite catalysts for the low temperature oxidation of CO, *Appl. Surf. Sci.* 257 (2011) 7551–7559.
- [48] J. Marrero-Jerez, A. Murugan, I.S. Metcalfe, P. Nunez, TPR-TPD-TPO studies on CGO/NiO and CGO/CuO ceramics obtained from freeze-dried precursors, *Ceram. Int.* 40 (2014) 15175–15182.
- [49] J. Choi, H. Oh, S.-W. Han, S. Ahn, J. Noh, J.B. Park, Preparation and characterization of graphene oxide supported Cu, Cu<sub>2</sub>O, and CuO nanocomposites and their high photocatalytic activity for organic dye molecule, *Curr. Appl. Phys.* 17 (2017) 137–145.
- [50] H. Jae-Hoon, K. Seung Hyun, C. Jae Hwan, K. Sung Youb, K. Ji Hyun, K. Soon-Yong, Enhancement of seawater corrosion resistance in copper using acetone-derived graphene coating, *Nanoscale* 6 (2014) 167–174.
- [51] X. Li, Y. Wang, J. Zhao, H. Wang, B. Wang, J. Huang, S. Deng, G. Yu, Electro-peroxide treatment of the antidepressant venlafaxine: operational parameters and mechanism, *J. Hazard. Mater.* 300 (2015) 298–306.
- [52] O.S.G.P. Soares, A.G. Goncalves, J.J. Delgado, J.J.M. Orfao, M.F.R. Pereira, Modification of carbon nanotubes by ball-milling to be used as ozonation catalysts, *Catal. Today* 249 (2015) 199–203.
- [53] H. Chen, Z. Zhang, Z. Yang, Q. Yang, B. Li, Z. Bai, Heterogeneous fenton-like catalytic degradation of 2,4-dichlorophenoxyacetic acid in water with FeS, *Chem. Eng. J.* 273 (2015) 481–489.
- [54] L. Zhang, Z. Xia, Mechanisms of oxygen reduction reaction on nitrogen-doped graphene for fuel cells, *J. Phys. Chem. C* 115 (2011) 11170–11176.
- [55] W. Chen, Y. Bao, X. Li, J. Huang, J. Xie, L. Li, Role of Si-F groups in enhancing interfacial reaction of Fe-MCM-41 for pollutant removal with ozone, *J. Hazard. Mater.* 393 (2020).
- [56] J. Cao, L. Lai, B. Lai, G. Yao, X. Chen, L. Song, Degradation of tetracycline by peroxymonosulfate activated with zero-valent iron: performance, intermediates, toxicity and mechanism, *Chem. Eng. J.* 364 (2019) 45–56.
- [57] Y. Wang, H. Zhang, L. Chen, S. Wang, D. Zhang, Ozonation combined with ultrasound for the degradation of tetracycline in a rectangular air-lift reactor, *Sep. Purif. Technol.* 84 (2012) 138–146.